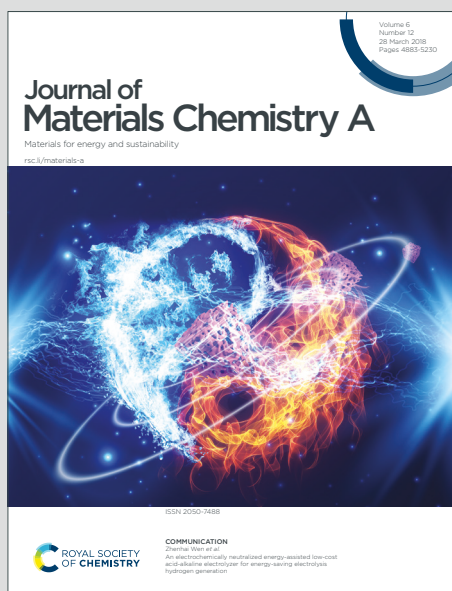


Journal of Materials Chemistry A

Materials for energy and sustainability

Accepted Manuscript

This article can be cited before page numbers have been issued, to do this please use: S. Ge, L. Yang, Z. wang, T. Du, Q. Guo, M. Liu, M. Du and E. Zhou, *J. Mater. Chem. A*, 2025, DOI: 10.1039/D5TA05058H.



This is an Accepted Manuscript, which has been through the Royal Society of Chemistry peer review process and has been accepted for publication.

Accepted Manuscripts are published online shortly after acceptance, before technical editing, formatting and proof reading. Using this free service, authors can make their results available to the community, in citable form, before we publish the edited article. We will replace this Accepted Manuscript with the edited and formatted Advance Article as soon as it is available.

You can find more information about Accepted Manuscripts in the [Information for Authors](#).

Please note that technical editing may introduce minor changes to the text and/or graphics, which may alter content. The journal's standard [Terms & Conditions](#) and the [Ethical guidelines](#) still apply. In no event shall the Royal Society of Chemistry be held responsible for any errors or omissions in this Accepted Manuscript or any consequences arising from the use of any information it contains.

Tailoring Aggregation Behavior of Shamrock-shaped Non-fullerene Acceptors via Isomeric Strategy Enables High-Performance Organic Solar Cells

Sheng Ge^{1,2}, Lei Yang², Zongtao Wang¹, Tianfeng Du², Qing Guo^{2*}, Manying Liu⁴, Mengzhen Du³, Erjun Zhou^{3*}

¹ School of Materials Science and Engineering, Zhengzhou University, Zhengzhou 450001, China.

² Henan Institute of Advanced Technology, Zhengzhou University, Zhengzhou 450001, China

³ College of Biological and Chemical Engineering, Jiaying University, Jiaying 314001, China

⁴ College of Chemical and Materials Engineering, Xuchang University, Xuchang, Henan 461000, China.

E-mail: qingg319@zzu.edu.cn, zhouej@nanoctr.cn

Abstract

End-group halogenation strategy in banana-shaped Y-series non-fullerene acceptors (NFAs) play a crucial role in the development of organic solar cells (OSCs). Compared to fluorinated end-groups, chlorinated end-groups offer advantages such as simpler synthesis, lower cost, and higher open-circuit voltage (V_{OC}). In this study, we replaced the benzothiadiazole (BT) unit in Y-series molecules with an acenaphtho[1,2-b]quinoxaline imide (AQI) structure and utilized IC-*p*2Cl and IC-*o*2Cl isomers as end-groups respectively to synthesize two shamrock-shaped NFAs, AQI16 and AQI17. Further investigations revealed that the substitution position of chlorine atoms plays a critical role in modulating the π - π stacking and crystallinity of the materials. Besides, end-group isomerization significantly influences the photophysical and photovoltaic properties of the materials. D18:AQI16 combination achieved power conversion efficiency (PCE) of 17.90%, which is obviously higher than that of AQI17 based device (15.14%). This work highlights the impact of isomerization caused by halogen substitution positions on the photovoltaic properties of shamrock-shaped NFAs.



Keywords: Organic solar cells; acenaphtho[1,2-b]quinoxaline imide; end-group isomeric strategy; halogen substitution positions; non-fullerene acceptors

1. Introduction

Organic solar cells (OSCs), as an emerging photovoltaic technology, have demonstrated tremendous application potential in wearable electronics and building-integrated photovoltaics (BIPV) owing to their unique advantages including low-cost manufacturing, mechanical flexibility, solution processability, and semi-transparency¹⁻⁴. The core component features a bulk heterojunction (BHJ) active layer architecture, where nanoscale blending of donor and acceptor materials forms an interpenetrating network that facilitates efficient exciton dissociation and charge transport.⁵⁻⁷ In recent years, through synergistic innovations encompassing the development of novel photoactive materials, device engineering optimizations, and fundamental investigations into photophysical mechanisms, this technology has achieved a landmark power conversion efficiency (PCE) exceeding 20%⁸⁻¹². This transformative advancement is largely driven by the development of non-fullerene acceptors (NFAs)¹³⁻¹⁶. However, collaboratively optimize the open-circuit voltage (V_{OC}), short-circuit current density (J_{SC}), and fill factor (FF) continues to pose a formidable challenge for the scientific community.

Molecular configuration differences can significantly alter molecular packing patterns, and this structure-packing-property relationship directly affects active layer morphology formation and ultimate photovoltaic performance¹⁷⁻¹⁹. In 2015, Zhan et al, et al. first synthesized an S-shaped molecule ITIC with a donor acceptor donor (A-D-A) type NFA²⁰. The state-of-the-art ITIC-based acceptor materials typically demonstrate PCE around 15%. The performance primarily limited by two critical factors. First, their absorption edges generally fall below 800 nm, resulting in insufficient utilization of near-infrared solar photons and consequently limiting photogenerated exciton production. Second, the two aromatic side chains attached to



the sp^3 -hybridized carbon atom in ITIC-based NFAs create substantial steric hindrance, which significantly impedes intermolecular interactions between the central cores and ultimately limits further improvements in device performance. Building upon this foundation, Zou et al, achieved another milestone in 2019 by developing Y6, a banana shaped NFA with A-DA'D-A structured²¹. Benefiting from superior intramolecular charge-transfer (ICT) effects and favorable 3D molecular packing of these Y-series acceptors, combined with synergistic optimization of molecular structure and device engineering, the PCE of Y-type materials has now surpassed 20% with an impressive J_{SC} over 28 mA/cm² and FF of 0.8. However, the V_{OC} remains relatively modest²²⁻²⁴. The study demonstrates that replacing the benzothiadiazole (BT) unit in the central core with quinoxaline (Qx) structures and their derivatives can enhance the quinoidal resonance effect, promote intermolecular π - π stacking, improve charge transport properties, and reduce reorganization energy, thereby increasing both J_{SC} and FF^{17, 25}. Furthermore, extending the Qx structure into two dimensions (2D) can strengthen molecular packing and enhance material crystallinity. As π -conjugated systems, imide derivatives exhibit excellent planarity, rigidity, and thermal stability, making them a class of organic optoelectronic materials with unique photophysical and chemical properties^{15, 26}. Based on core unit regulation, which plays a decisive role in ICT effect, adjusting molecular orbital energy levels and modifying molecular packing, shamrock-shaped NFAs were developed. In our previous work, two shamrock-shaped NFAs, AQI2 and AQI4 were developed by incorporating acenaphtho[1,2-b]quinoxaline imide (AQI) as a bulky A'-unit to replace the BT unit in Y6²⁷⁻²⁹. It has proved that NFAs containing the AQI unit exhibit enhanced luminescence, reduced Stokes shift, and lower energy loss. The molecular design strategy of these shamrock-shaped NFAs unveils a promising pathway toward high-efficiency OSCs with superior V_{OC} . Furthermore, this category of acceptors warrants in-depth investigation in combination with other optimization approaches to elucidate the structure-property correlations.

Precise structural modulation of AQI-based materials and in-depth investigation of their structure-property relationships are of paramount importance for developing high-performance photovoltaic materials. End-group modification can effectively



modulate materials properties such as molecular energy levels, intermolecular interactions and molecular packing behavior Remarkably, halogen atoms particularly fluorine (F) and chlorine (Cl) constitute the predominant choice in molecular design³⁰⁻⁴⁰. Notably, Cl substitution demonstrates distinctive advantages over its F counterpart: 1) more chemically reactive and cost-effective, 2) superior polarizability (Cl: 2.18 Å³ vs F: 0.56 Å³) enabling dynamic induction effects that boost intramolecular charge separation efficiency, 3) balanced electronegativity that prevents excessive open-circuit voltage loss, 4) strengthened intramolecular charge transfer effects inducing bathochromic shifts in absorption spectra with concomitant extinction coefficient increases⁴¹⁻⁴⁴. In addition, the positional arrangement of Cl substituents plays a critical role in governing material performance^{26, 45-51}. Hence, the structural evolution not only fine-tunes optoelectronic properties but also opens new avenues for optimizing charge transport and morphological stability in high-performance OSCs.

To sum up, further optimization of AQI-type NFAs through end-group engineering has been achieved to realize enhanced photovoltaic performance. We successfully synthesized two novel NFAs, AQI16 and AQI17, with two isomeric units 2-(4,5-dichloro-3-oxo-2,3-dihydro-1H-inden-1-ylidene)malononitrile (IC-*o*2Cl) and 2-(5,6-Dichloro-3-oxo-2,3-dihydro-1H-inden-1-ylidene)malononitrile (IC-*p*2Cl). Studies revealed that the variation in the substitution position of chlorine atoms significantly influenced the photophysical properties and photovoltaic performance of the AQI-based acceptor. Compared to AQI16, AQI17 exhibited a higher lowest unoccupied molecular orbital (LUMO) energy level, which, when paired with the donor material D18, resulted in a high V_{OC} of 0.975 V. On the other hand, AQI16 demonstrated stronger π - π stacking in the aggregated state, leading to a broader absorption range and superior crystallinity. The device based on D18:AQI16 achieved a PCE of 17.9%, with a J_{SC} of 25.2 mA cm⁻² and an FF of 74.4%.

2. Results and discussion

The molecular structures of D18, AQI16 and AQI17 are displayed in Figure 1a, and the elaborated synthetic pathways of AQI16 and AQI17 in Scheme S1 in supporting



information. The isomeric AQI16 and AQI17 shared an identical central core but different substitution positions of chlorine atoms on their terminal groups. To unravel the influence of chlorine substitution patterns on molecular properties, density functional theory (DFT) calculations were conducted at the B3LYP/6-31G (d) level. As shown in Figure S1 the AQI16 and AQI17 display overall dipole moments of 1.27 D and 2.39 D, respectively. Data confirm that both NFAs adopt planar configurations, conducive to robust π - π stacking and high crystallinity. Figure 2b maps the electrostatic surface potential (ESP) of AQI16 and AQI17, revealing distinct ESP redistributions driven by chlorine substitution. The terminal region of AQI16 exhibits a more positive ESP relative to AQI17.

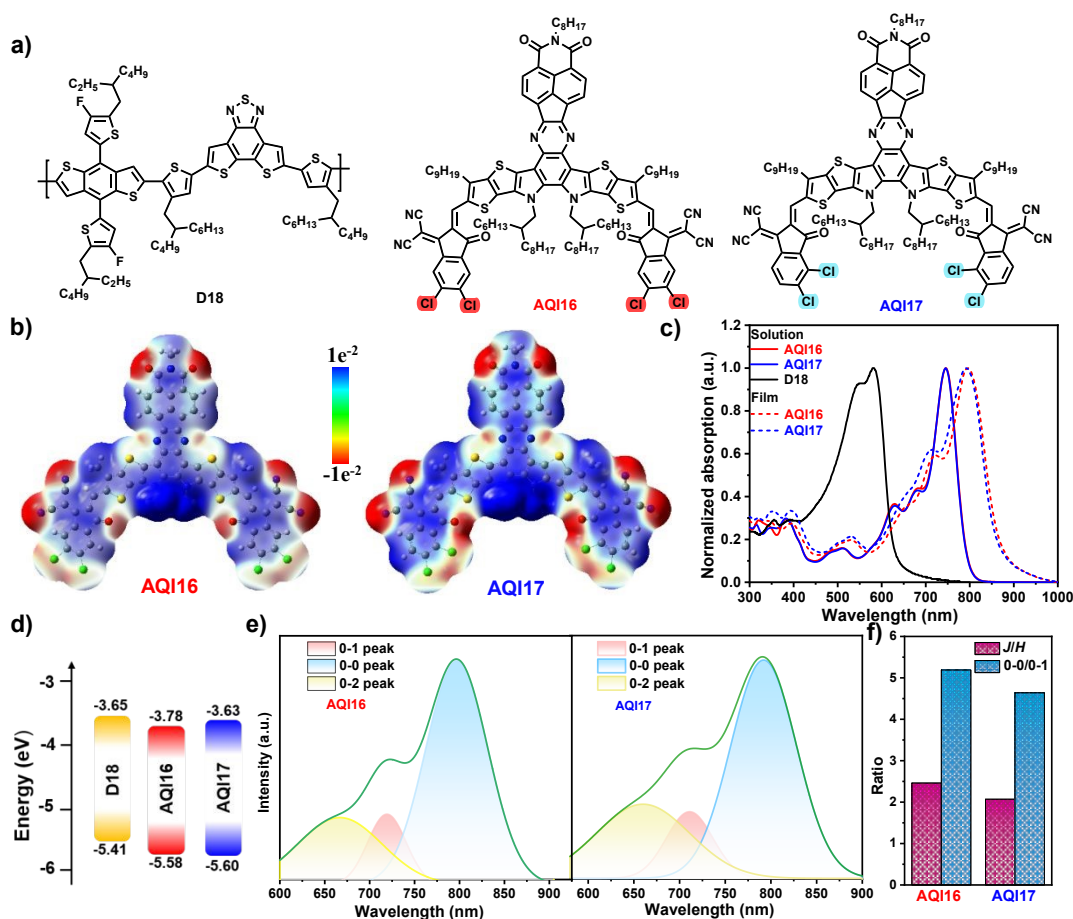


Figure 1. a) Molecular structures of D18, AQI16, and AQI17. b) Electrostatic surface potential distribution of AQI16 and AQI17. c) UV-Vis absorption spectra of D18, AQI16 and AQI17. d) Energy levels of D18, AQI16, and AQI17. e) Energy alignment diagram of AQI16 and AQI17. f) The statistic J/H and 0-0/0-1 intensity ratios.

Table 1. Summary of the photophysical and electrochemical properties of AQI16 and



AQI17.

View Article Online
DOI: 10.1039/D5TA05058H

Acceptor	E_{HOMO} [eV]	E_{LUMO} [eV]	$\lambda_{\text{max, sol}}$ [nm]	$\lambda_{\text{max, film}}$ [nm]	$\lambda_{\text{onset, film}}$ [nm]	$^a E_{\text{g}}^{\text{opt}}$ [eV]
AQI16	-5.58	-3.78	745	796	887	1.40
AQI17	-5.60	-3.63	745	790	877	1.41

^a) Calculation: $E_{\text{g}}^{\text{opt}} = 1240/\lambda_{\text{onset, film}}$ (eV)

Cyclic voltammetry (CV) measurements evaluate the difference in photoelectron characteristics of the two acceptors. As depicted in Figure 1b, the HOMO/LUMO of AQI16 and AQI17 are -5.58/-3.78 eV and -5.60/-3.74 eV, respectively. The higher LUMO energy of AQI17 contributes to enhanced V_{OC} . And the HOMO/LUMO of D18 locates at -5.41/-3.65 eV. The energy offset between the donor and acceptor enables efficient exciton dissociation. The UV-Vis absorption spectra of the NFAs, AQI16 and AQI17, are shown in Figure 1c and the detailed parameters are displayed in Table 1. In solution, both AQI16 and AQI17 display identical maximum absorption peaks at 745 nm. From solution to film state, the enhanced π - π interactions induce a pronounced redshift in the maximum absorption peak. The thin-film absorption peak for AQI16 and AQI17 are located at 796 nm and 790 nm, respectively. In addition, the 0-0, 0-1, and 0-2 peaks are fitted as shown in Figure 2e. The J/H aggregate ratios (determined by 0-0/0-2 transition area ratio) of AQI16 and AQI17 are 2.45 and 2.07, respectively. The higher values of AQI16 indicate the enhanced J -aggregate compared to AQI17. Besides, the 0-0/0-1 intensity ratios of AQI16 and AQI17 are 5.19 and 4.64, respectively, suggesting the increased intermolecular interaction in AQI16.

To gain a deeper understanding of the photovoltaic performance of the two NFAs, OSC devices were fabricated using a conventional structure: ITO/PEDOT:PSS/Active layer/PNDIT-F3N/Ag. Polymer D18 was selected as the electron donor in the active layer due to its suitable energy levels and complementary absorption properties. The weight ratio of D18 to the acceptor was 1:1.2, and the mixture was dissolved in chloroform. The specific parameters are listed in the corresponding table 2. From these results, it can be observed that the device based on AQI17 exhibits a higher V_{OC} of 0.975 eV compared to the device based on AQI16, which is primarily attributed to the higher



LUMO energy level of AQI17. While, AQI16 exhibits superior photon utilization efficiency, leading to a higher photocurrent density when combined with D18 compared to AQI17. And the J_{SC} of the D18:AQI16 and D18:AQI17 devices are measured at 25.2 and 21.70 mA cm^{-2} , respectively. As the result, D18:AQI16 based devices give an excellent PCE of 17.90% with an FF of 74.40%, which is higher than D18:AQI17 based device (PCE of 15.14% and FF of 69.95%). The external quantum efficiency (EQE) spectra of the D18:AQI16 and D18:AQI17 devices are illustrated in Figure 2b. The calculated J_{SC} values are in good consistent with the J_{SC} measured in $J-V$ curves depicted in Figure 2a. Specifically, the D18:AQI16 device achieves a maximum EQE of 88% at 525 nm, significantly surpassing the 81% EQE at 590 nm for D18:AQI17. The enhanced J -aggregation characteristics and intensified intermolecular interactions of AQI16 within the 600-800 nm spectral region are predominantly driven by halogen substitution position-dependent modulation of aggregation behavior. These EQE results validate the trends observed in the $J-V$ measurements. Figure 2c shows the efficiency histograms of two types of devices for observing the differences in device efficiency and demonstrating the excellent reproducibility of the D18:AQI16 and D18:AQI17-based devices. Devices fabricated with the PM6 donor exhibited identical trends, with the corresponding data presented in Figure S4 and table S1.

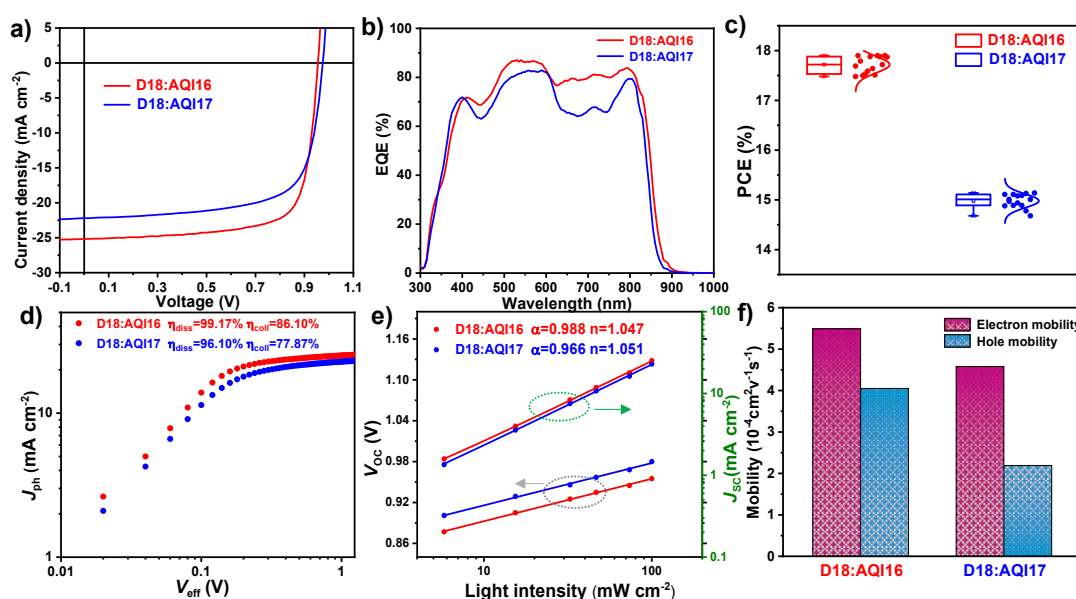


Figure 2. a) $J-V$ characteristics. b) EQE spectra. c) The average PCEs devices. d) J_{ph} versus V_{eff} plots. e) Dependence of J_{SC} and V_{OC} on the light intensity. f) Electron



and hole mobility.

View Article Online
DOI: 10.1039/D5TA05058H

Table 2. Photovoltaic parameters of the optimized D18:AQI16 and D18:AQI17 based devices under the illumination of AM 1.5 G, 100 mW cm⁻².

Active layer	V_{OC} (V)	$J_{SC}/^aJ_{cal}$ (mA/cm ²)	FF (%)	^b PCE (%)
D18:AQI16	0.955	25.20 / 23.94	74.40	17.90 (17.69±0.20)
D18:AQI17	0.975	22.20 / 21.70	69.95	15.14 (14.91±0.21)

^a) Integrated from EQE curves.

^b) Average data from over 15 independent devices.

To further explore the differences in J_{SC} , V_{OC} , and PCE between D18:AQI16 and D18:AQI17 devices, we studied the exciton dissociation, recombination, and charge carrier dynamics. As shown in Figure 2d, the photocurrent density (J_{ph}) was calculated as the difference between the current density under illumination (J_L) and in the dark (J_D): $J_{ph} = J_L - J_D$. By plotting J_{ph} against the effective voltage (V_{eff}), defined as $V_{eff} = V_0 - V_A$, (where V_0 is the voltage at $J_{ph}=0$ and V_A is the applied external bias), we evaluated the charge generation and extraction efficiency. Assuming an external bias of 1.24 V, at which all excitons are dissociated and collected, the saturated J_{ph} was obtained. Using the equation $\eta_{diss} = \frac{J_{sc}}{J_{ph}}$, the exciton dissociation probabilities for the D18:AQI16 and D18:AQI17 devices were calculated to be 99.17% and 96.10%, respectively. Furthermore, under short-circuit and maximum power output conditions, the exciton dissociation efficiencies for the D18:AQI16 and D18:AQI17 devices were calculated to be 86.57% and 77.78%, respectively, using the equation $\eta_{coll} = \frac{J_{max\ power}}{J_{ph}}$. Therefore, D18:AQI16 outperforms D18:AQI17 in terms of photon capture capability and exciton dissociation/collection efficiency, which is one of the primary reasons for the higher J_{SC} observed in the D18:AQI16 -based device.

To further explore the influence of end-group isomerization on device performance, dark J - V characteristics were analyzed, and rectification ratios were computed under forward and reverse bias conditions. Within the voltage range of -0.5 to 0 V, the D18:AQI16 device exhibits a notably lower reverse current compared to



D18:AQI17, signifying reduced leakage current, as shown in Figure S5. The rectification ratios for D18:AQI16 and D18:AQI17 are determined to be 29,709 and 3,616, respectively. The higher rectification ratio of D18:AQI16 underscores its enhanced charge selectivity and superior interfacial contact properties.

The charge recombination behavior in the two devices is studied by measuring the curves of J_{SC} and V_{OC} versus the light intensity (P_{light}). The relationship between J_{SC} and P_{light} can be evaluated by the formula of $J_{SC} \propto P_{light}^{\alpha}$, where the α represents the exponential factor. The value of α closer to 1 indicates weaker bimolecular recombination effects in the blended film. As shown in the Figure 2e, the α value for D18:AQI16 is 0.988, significantly closer to 1 compared to 0.966 for D18:AQI17. The relationship between V_{OC} and P_{light} follows the formula of $V_{OC} \propto \frac{nkT}{q} \ln P_{light}$, where k , T , and q are the Boltzmann constant, Kelvin temperature, and elementary charge, respectively. When the slope of the line approaches kT/q , trap-assisted recombination in the blended film is suppressed. The slopes for devices based on D18:AQI16 and D18:AQI17 are $1.047 kT/q$ and $1.051 kT/q$, respectively, indicating the weaker trap-assistant recombination in D18:AQI16 based device. In addition, the charge carrier transport properties of the D18:AQI16 and D18:AQI17 devices were investigated using the space-charge-limited current (SCLC) method, as shown in Figure S6. The corresponding parameters are displayed in Figure 2f, the electron and hole mobilities of D18:AQI16 are 5.49×10^{-4} and $4.15 \times 10^{-4} \text{ cm}^2 \text{ v}^{-1} \text{ s}^{-1}$, respectively. Compared to D18:AQI17 4.58×10^{-4} and $2.19 \times 10^{-4} \text{ cm}^2 \text{ v}^{-1} \text{ s}^{-1}$, the $\frac{\mu_h}{\mu_e}$ ratio of D18:AQI16 is closer to 1. Consequently, the more suppressed recombination behavior, improved charge transport and more balanced charge mobilities attribute to the higher J_{SC} and FF of the D18:AQI16 based OSCs.



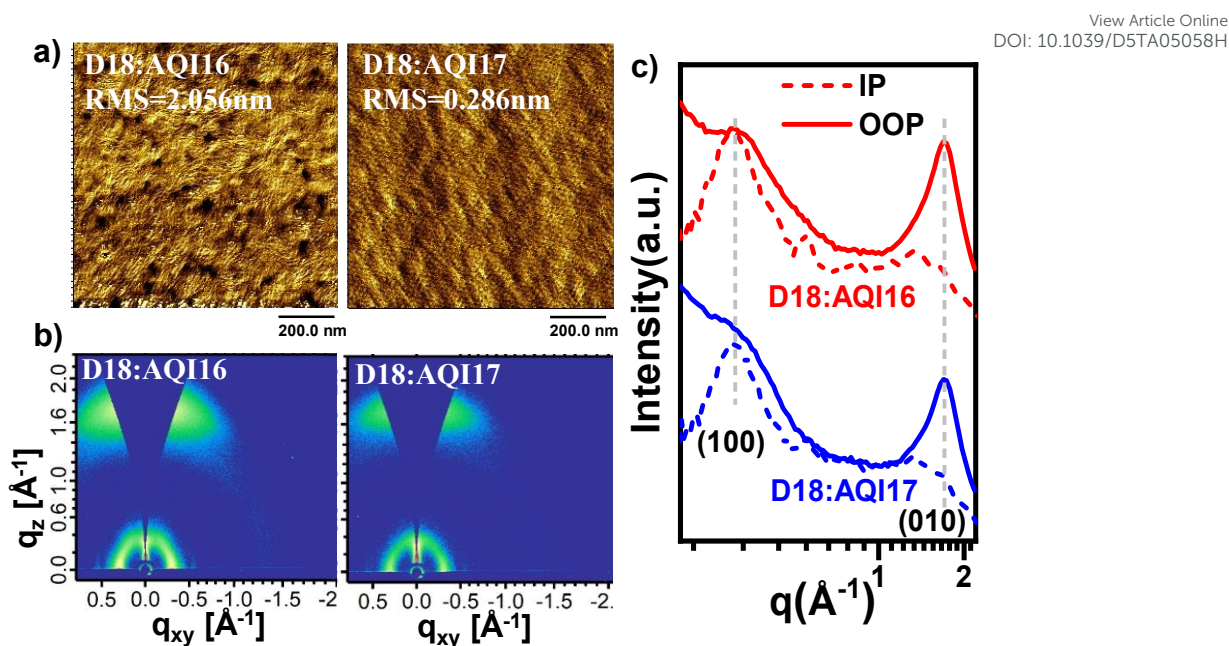


Figure 3. a) AFM phase image. b) 2D GIWAXS patterns and c) intensity profiles along the IP and OOP directions.

The morphology of active layer was subsequently analyzed using atomic force microscopy (AFM) as shown in Figure 3a. Both films exhibit fine nanoscale morphology, which is highly favorable for efficient charge separation and transport. The root mean square (RMS) roughness of the D18:AQI16 blend film is 2.056 nm, significantly higher than that of the D18:AQI17 blend film (0.286 nm), which may attribute to the superior crystallinity of AQI16. To further investigate the influence of halogen substitution positions on molecular stacking in BHJ films, Figures 3b-c presents the two-dimensional grazing-incidence wide-angle X-ray scattering (GIWAXS) patterns and corresponding line-cut intensity profiles for D18:AQI16 and D18:AQI17. Prominent (010) diffraction peaks are observed in the out-of-plane (OOP) direction for both blend films, indicating strong π - π stacking in the face-on direction, which enhances charge transport and collection. In addition, the (010) diffraction peaks along the OOP direction for D18:AQI16 and D18:AQI17 are located at 1.706 and 1.703 \AA^{-1} , respectively. The corresponding π - π stacking distances ($d_{\pi-\pi}$) were calculated to be 3.681 and 3.688 \AA . The tighter molecular packing in D18:AQI16 enables more efficient charge transport. The crystallite coherence lengths (CCL) were calculated using the



Scherrer equation ($CCL = \frac{2\pi}{FWHM}$, where FWHM is the full width at half maximum of the peak). For the (100) diffraction peaks in-plane (IP) direction, the CCL values of D18:AQI16 and D18:AQI17 are 64.180 and 62.800 Å, respectively, indicating that D18:AQI16 exhibits superior phase separation. Additional detailed parameters are provided in table S4.

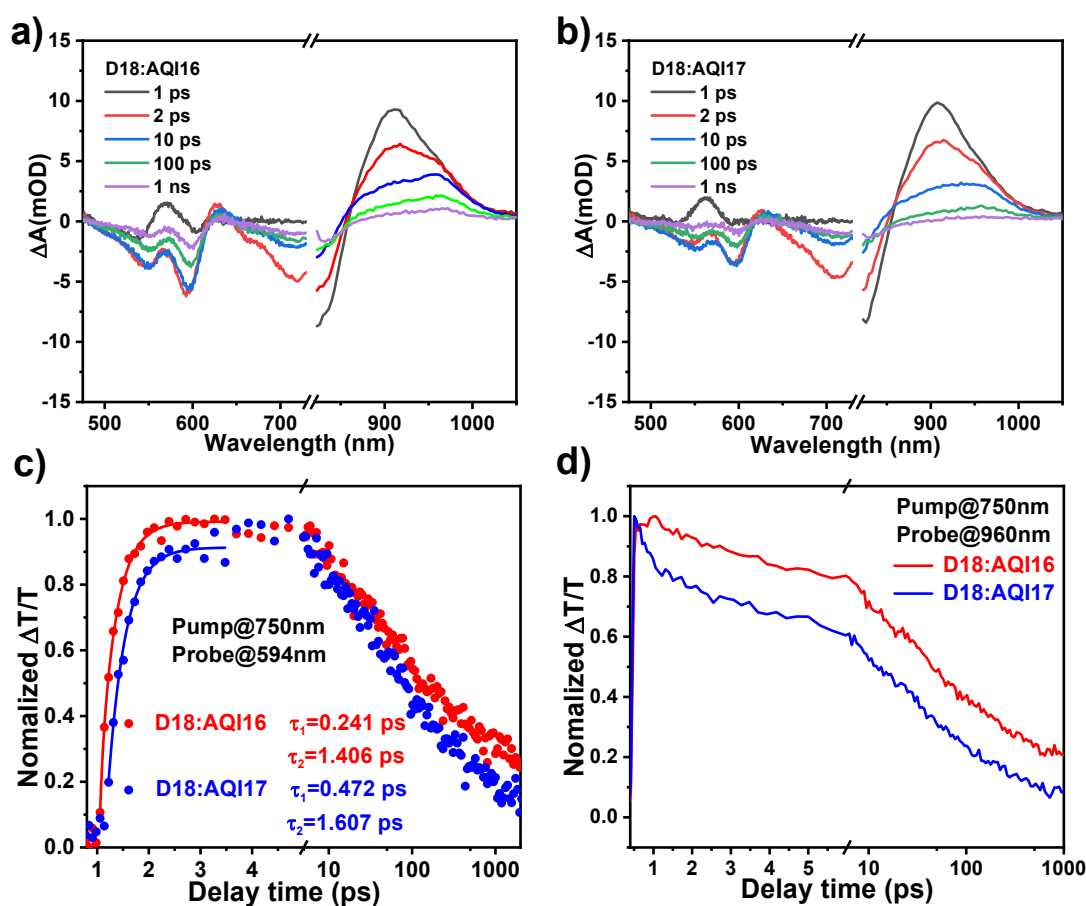


Figure 4. a, b) TA spectra recorded at different time delays. c) Decay profiles probed. d) Exciton dynamics probed.

To investigate the impact of end-group isomerization on carrier dynamics in OSCs, femtosecond transient absorption (fs-TA) spectroscopy was employed to probe exciton dissociation, transport, and recombination. A 750 nm pump pulse was selected to selectively excite the acceptor materials. Figure S8 presents the TA colormaps of the D18:AQI16 and D18:AQI17 blend films, with corresponding kinetic traces shown in Figures 4a-b. In both blend films, ground-state bleaching (GSB) signals emerge in the 650-850 nm range upon photoexcitation, followed by hole transfer from the acceptor to



the donor (D18) within a 1 ns timescale. Concurrently, similar GSB signals observed in the 540-610 nm region are attributed to the absorption of the polymer donor D18. Additionally, positive signals in the 870-1000 nm range arise from the excited-state absorption (ESA) of the small-molecule acceptors. The exciton dissociation dynamics at 594 nm were analyzed by fitting the kinetic traces with a biexponential function to extract lifetimes τ_1 and τ_2 , as shown in Figure 4c and table S5. The τ_1 and τ_2 indicated the ultrafast exciton dissociation at the interface and exciton diffusion in the domains, respectively. D18:AQI16 exhibited $\tau_1=0.241$ ps and $\tau_2=1.406$ ps, while D18:AQI17 showed $\tau_1=0.472$ ps and $\tau_2=1.607$ ps. The data reveal that D18:AQI16 film presents the faster exciton dissociation and diffusion, which is primarily attributed to the superior crystallization and ordered packing structure. Besides, longer charge transfer state lifetimes can be observed by the slower attenuation of donor GSB peak in D18:AQI16 based films, which indicates less charge recombination, leading to the higher J_{SC} and FF in the corresponding device. Besides, Figure 4d suggest that the rate of exciton recombination is faster in the D18:AQI17 mixed film. These results highlight the critical role of end-group isomerization in modulating exciton dynamics and interfacial charge separation efficiency in OSCs.

3. Conclusion

In summary, we initially substituted the BT unit in the A'-unit of Y-series acceptor materials with an AQI and synthesized two novel small-molecule acceptors, AQI16 and AQI17, with different substitution positions of chlorine atoms in the end groups. The substitution position of chlorine atoms plays a critical role in modulating the π - π stacking and crystallinity of the materials. When paired with the donor material D18, the D18:AQI16-based OSC achieved a superior PCE of 17.9% with a J_{SC} of 25.2 mA cm⁻² and an FF of 74.4%. While, the D18:AQI17-based device gave a relative lower PCE of 15.14%. The superior photovoltaic performance of D18:AQI16 can be attributed to its enhanced exciton dissociation kinetics, improved charge transport properties, and favorable active layer morphology. These results underscore the critical role of end-group isomerization engineering in tailoring the optoelectronic and



aggregation behaviors of NFAs, providing a strategic pathway for high-performance OSCs.

Supporting Information

The data that support the findings of this study are available from the corresponding author upon reasonable request.

Conflicts of interest

There are no conflicts to declare.

Acknowledgements

The authors thank the support from the National Natural Science Foundation of China (52303259; 52373176).

References

1. W. Song, B. Fanady, R. Peng, L. Hong, L. Wu, W. Zhang, T. Yan, T. Wu, S. Chen and Z. Ge, *Adv. Energy Mater.*, 2020, **10**, 200136.
2. L. Meng, Y. Zhang, X. Wan, C. Li, X. Zhang, Y. Wang, X. Ke, Z. Xiao, L. Ding, R. Xia, H.-L. Yip, Y. Cao and Y. Chen, *Science*, 2018, **361**, 1094-1098.
3. S. Guan, Y. Li, K. Yan, W. Fu, L. Zuo and H. Chen, *Adv. Mater.*, 2022, **34**, 2205844.
4. X. Chen, G. Xu, G. Zeng, H. Gu, H. Chen, H. Xu, H. Yao, Y. Li, J. Hou and Y. Li, *Adv. Mater.*, 2020, **32**, 1908478.
5. J. Hou, O. Inganäs, R. H. Friend and F. Gao, *Nat. Mater.*, 2018, **17**, 119-128.
6. M. Xie, Z. Wei and K. Lu, *Chem. Sci.*, 2024, **15**, 8265-8279.
7. G. Zhang, F. R. Lin, F. Qi, T. Heumüller, A. Distler, H.-J. Egelhaaf, N. Li, P. C. Y. Chow, C. J. Brabec, A. K. Y. Jen and H.-L. Yip, *Chem. Rev.*, 2022, **122**, 14180-14274.
8. L. Zhu, M. Zhang, G. Zhou, Z. Wang, W. Zhong, J. Zhuang, Z. Zhou, X. Gao, L. Kan, B. Hao, F. Han, R. Zeng, X. Xue, S. Xu, H. Jing, B. Xiao, H. Zhu, Y. Zhang and F. Liu, *Joule*, 2024, **8**, 3153-3168.
9. C. Chen, L. Wang, W. Xia, K. Qiu, C. Guo, Z. Gan, J. Zhou, Y. Sun, D. Liu, W. Li and T. Wang, *Nat. Commun.*, 2024, **15**, 6865.
10. Y. Jiang, S. Sun, R. Xu, F. Liu, X. Miao, G. Ran, K. Liu, Y. Yi, W. Zhang and X. Zhu, *Nat. Energy*, 2024, **9**, 975-986.
11. Y. Sun, L. Wang, C. Guo, J. Xiao, C. Liu, C. Chen, W. Xia, Z. Gan, J. Cheng, J. Zhou, Z. Chen, J. Zhou, D. Liu, T. Wang and W. Li, *J. Am. Chem. Soc.*, 2024, **146**, 12011-12019.
12. J. Zhu, R. Zeng, E. Zhou, C. Li, J. Deng, M. Du, Q. Guo, M. Ji, Z. Wang, Y. Lin, F. Han, J. Zhuang, S. Tan, L. Kan, L. Zhu, M. Zhang and F. Liu, *J. Am. Chem. Soc.*, 2025, DOI: 10.1021/jacs.5c04656,



<https://doi.org/10.1021/jacs.1025c04656>.

View Article Online
DOI: 10.1039/D5TA05058H

13. H. Liu, Y. Geng, Z. Xiao, L. Ding, J. Du, A. Tang and E. Zhou, *Adv. Mater.*, 2024, **36**, 2404660.
14. K. Liu, Y. Jiang, G. Ran, F. Liu, W. Zhang and X. Zhu, *Joule*, 2024, **8**, 835-851.
15. Y. Lang, H. Lai, Y. Fu, R. Ma, P. W. K. Fong, H. Li, K. Liu, X. Yang, X. Lu, T. Yang, G. Li and F. He, *Adv. Mater.*, 2024, **37**, 2413270.
16. R. Xu, Y. Jiang, F. Liu, G. Ran, K. Liu, W. Zhang and X. Zhu, *Adv. Mater.*, 2024, **36**, 2312101
17. H. Bi, D. Qiu, H. Zhang, C. Wang, M. Wu, X. Ran, J. Zhang, Y. Wang, A. Tang, X. Miao, Z. Wei and K. Lu, *Chem. Eng. J.*, 2025, **506**, 159972.
18. H. He, X. Li, J. Zhang, Z. Chen, Y. Gong, H. Zhuo, X. Wu, Y. Li, S. Wang, Z. Bi, B. Song, K. Zhou, T. Liang, W. Ma, G. Lu, L. Ye, L. Meng, B. Zhang, Y. Li and Y. Li, *Nat. Commun.*, 2025, **16**, 787.
19. Y. Jiang, K. Liu, F. Liu, G. Ran, M. Wang, T. Zhang, R. Xu, H. Liu, W. Zhang, Z. Wei, Y. Cui, X. Lu, J. Hou and X. Zhu, *Adv. Mater.*, 2025, **37**, 2500282.
20. Y. Lin, J. Wang, Z. G. Zhang, H. Bai, Y. Li, D. Zhu and X. Zhan, *Adv. Mater.*, 2015, **27**, 1170-1174.
21. J. Yuan, Y. Zhang, L. Zhou, G. Zhang, H.-L. Yip, T.-K. Lau, X. Lu, C. Zhu, H. Peng, P. A. Johnson, M. Leclerc, Y. Cao, J. Ulanski, Y. Li and Y. Zou, *Joule*, 2019, **3**, 1140-1151.
22. F. Liu, Y. Jiang, R. Xu, W. Su, S. Wang, Y. Zhang, K. Liu, S. Xu, W. Zhang, Y. Yi, W. Ma and X. Zhu, *Angew. Chem. Int. Ed.*, 2023, **63**, e202313791.
23. S. Guan, Y. Li, C. Xu, N. Yin, C. Xu, C. Wang, M. Wang, Y. Xu, Q. Chen, D. Wang, L. Zuo and H. Chen, *Adv. Mater.*, 2024, **36**, 2400342.
24. Z. Chen, J. Ge, W. Song, X. Tong, H. Liu, X. Yu, J. Li, J. Shi, L. Xie, C. Han, Q. Liu and Z. Ge, *Adv. Mater.*, 2024, **36**, 2406690.
25. W. Wei, C. e. Zhang, Z. Chen, W. Chen, G. Ran, G. Pan, W. Zhang, P. Müller - Buschbaum, Z. Bo, C. Yang and Z. Luo, *Angew. Chem. Int. Ed.*, 2024, **63**, e202315625.
26. K. Liu, Y. Jiang, F. Liu, G. Ran, F. Huang, W. Wang, W. Zhang, C. Zhang, J. Hou and X. Zhu, *Adv. Mater.*, 2023, **35**, 2300363.
27. Z. Wang, M. Ji, A. Tang, M. Du, C. Mu, Y. Liu, E. Wang and E. Zhou, *Energy Environ. Sci.*, 2024, **17**, 3868-3877.
28. X. Zhang, Q. Guo, Z. Wang, J. Song, Z. Zheng, J. Han and E. Zhou, *Chin. J. Chem.*, 2025, **43**, 2441-2448.
29. S. Xia, J. Xu, Z. Wang, S. Lee, L. Wang, Y. Hu, X. Zhao, C. Yang, E. Zhou and Z. Yuan, *Angew Chem Int Ed Engl*, 2025, **64**, e202501816.
30. J. Tao, K. Yang, D. Qiu, C. Wang, H. Zhang, M. Lv, J. Zhang, K. Lu and Z. Wei, *Nano Energy*, 2024, **125**, 109540.
31. Y. Zhang, Y. Li, R. Peng, Y. Qiu, J. Shi, Z. Chen, J. Ge, C. Zhang, Z. Tang and Z. Ge, *J. Energy Chem.*, 2024, **88**, 461-468.
32. X. Xu, C. Sun, J. Jing, T. Niu, X. Wu, K. Zhang, F. Huang, Q. Xu, J. Yuan, X. Lu, Y. Zhou and Y. Zou, *ACS Appl. Mater. Interfaces*, 2022, **14**, 36582-36591.
33. Z. Li, Z. a. Xu, S. Chen, J. Yao, H. Fu, M. Zhang, Y. Bai, H. Wang, Z. Liu and Z.-G. Zhang, *J. Mater. Chem. A*, 2023, **11**, 4539-4546.
34. T. Dai, Y. Meng, Z. Wang, J. Lu, Z. Zheng, M. Du, Q. Guo and E. Zhou, *J. Am. Chem. Soc.*, 2025, **147**, 4631-4642.
35. P. Cong, M. Du, A. Tang, X. Li, Z. Zheng, Y. Lei, Q. Guo, X. Sun, D. Deng and E. Zhou, *Macromolecules*, 2025, **58**, 704-715.
36. H. Lai, H. Chen, Y. Shen, M. Wang, P. Chao, W. Xie, J. Qu, B. Yang and F. He, *ACS Appl. Energy*



Mater., 2019, **2**, 7663-7669.

View Article Online
DOI: 10.1039/D5TA05058H

37. Q. Zhao, J. Qu and F. He, *Adv. Sci.*, 2020, **7**, 2000509.
38. C. Zhu, K. An, W. Zhong, Z. Li, Y. Qian, X. Su and L. Ying, *Chem. Commun.*, 2020, **56**, 4700-4703.
39. H. Chen, H. Liang, Z. Guo, Y. Zhu, Z. Zhang, Z. Li, X. Cao, H. Wang, W. Feng, Y. Zou, L. Meng, X. Xu, B. Kan, C. Li, Z. Yao, X. Wan, Z. Ma and Y. Chen, *Angew. Chem. Int. Ed.*, 2022, **61**, e202209580
40. H. Chen, Y. Zou, H. Liang, T. He, X. Xu, Y. Zhang, Z. Ma, J. Wang, M. Zhang, Q. Li, C. Li, G. Long, X. Wan, Z. Yao and Y. Chen, *Sci. China Chem.*, 2022, **65**, 1362-1373.
41. H. Lu, H. Jin, H. Huang, W. Liu, Z. Tang, J. Zhang and Z. Bo, *Adv. Funct. Mater.*, 2021, **31**, 2103445.
42. H. Liang, H. Chen, P. Wang, Y. Zhu, Y. Zhang, W. Feng, K. Ma, Y. Lin, Z. Ma, G. Long, C. Li, B. Kan, Z. Yao, H. Zhang, X. Wan and Y. Chen, *Adv. Funct. Mater.*, 2023, **33**, 2301573.
43. Q. Yang, H. Chen, J. Lv, P. Huang, D. Han, W. Deng, K. Sun, M. Kumar, S. Chung, K. Cho, D. Hu, H. Dong, L. Shao, F. Zhao, Z. Xiao, Z. Kan and S. Lu, *Adv. Sci.*, 2023, **10**, 2207678.
44. G. Zhang, Q. Wu, Y. Duan, W. Liu, M. Zou, H. Zhou, J. Cao, R. Li, X. Xu, L. Yu and Q. Peng, *Chem. Eng. J.*, 2023, **476**, 146538.
45. M. R. Busireddy, T.-W. Chen, S.-C. Huang, Y.-J. Su, Y.-M. Wang, W.-T. Chuang, J.-T. Chen and C.-S. Hsu, *ACS Appl. Mater. Interfaces*, 2022, **14**, 41264-41274.
46. J. Lv, Q. Yang, W. Deng, H. Chen, M. Kumar, F. Zhao, S. Lu, H. Hu and Z. Kan, *Chem. Eng. J.*, 2023, **465**, 142822.
47. H. Wu, B. Zhao, S. Zhang, Z. Bi, W. Wang, L. Wang, Z. Cong, W. Ma and C. Gao, *ACS Appl. Mater. Interfaces*, 2023, **15**, 14369-14378.
48. M. Xie, Y. Shi, L. Zhu, J. Zhang, Q. Cheng, H. Zhang, Y. Yan, M. Zhu, H. Zhou, K. Lu and Z. Wei, *Energy Environ. Sci.*, 2023, **16**, 3543-3551.
49. Q. Yang, D. Hu, M. Kumar, H. Dong, S. Ahmed, P. Huang, Z. Xiao and S. Lu, *Sol. RRL*, 2023, **7**, 2201062.
50. J. Fu, Q. Yang, P. Huang, S. Chung, K. Cho, Z. Kan, H. Liu, X. Lu, Y. Lang, H. Lai, F. He, P. W. K. Fong, S. Lu, Y. Yang, Z. Xiao and G. Li, *Nat. Commun.*, 2024, **15**, 1830.
51. H. Lai, Y. Zhu, Y. Ouyang, X. Lai, M. Ou, Z. Deng, Y. Wang, D. Qiu, C. Zhang and F. He, *Adv. Funct. Mater.*, 2024, **14**, 2418106.



Data Availability Statement

View Article Online
DOI: 10.1039/D5TA05058H

All relevant data are within the main text and the ESI† of this article.

